JACS
JOURNAL OF THE AMERICAN CHEMICAL SOCIETY
Article
Cite This: J. Am. Chem. Soc. XXXX, XXX, XXX−XXX
pubs.acs.org/JACS

Gold Nanocrystal Etching as a Means of Probing the Dynamic Chemical Environment in Graphene Liquid Cell Electron Microscopy

Matthew R. Hauwiller,[†] Justin C. Ondry,[†] Cindy M. Chan,[†] Prachi Khandekar,[†] Jessica Yu,[†] and A. Paul Alivisatos*[,†,‡,§,∥]

[†]Department of Chemistry and [‡]Department of Materials Science and Engineering, University of California—Berkeley, Berkeley, California 94720, United States

[§]Materials Sciences Division, Lawrence Berkeley National Laboratory, Berkeley, California 94720, United States

[∥]Kavli Energy NanoScience Institute, University of California-Berkeley and Lawrence Berkeley National Laboratory, Berkeley, California 94720, United States

Supporting Information

ABSTRACT: Graphene liquid cell electron microscopy has the necessary temporal and spatial resolution to enable the in situ observation of nanoscale dynamics in solution. However, the chemistry of the solution in the liquid cell during imaging is as yet poorly understood due to the generation of a complex mixture of radiolysis products by the electron beam. In this work, the etching trajectories of nanocrystals were used as a probe to determine the effect of the electron beam dose rate and preloaded etchant, $FeCl_3$, on the chemistry of the liquid cell. Initially, illuminating the sample at a low electron beam dose rate generates hydrogen bubbles, providing a reservoir of sacrificial reductant. Increasing the electron beam dose rate leads to a constant etching rate that varies linearly with the electron beam dose rate. Comparing these results with the oxidation potentials of the species in solution, the electron beam likely controls the total concentration of oxidative species in solution and $FeCl_3$ likely controls the relative ratio of oxidative species, independently determining the etching rate and chemical potential of the reaction, respectively. Correlating these liquid cell etching results with the ex situ oxidative etching of gold nanocrystals using $FeCl_3$ provides further insight into the liquid cell chemistry while corroborating the liquid cell dynamics with ex situ synthetic behavior. This understanding of the chemistry in the liquid cell will allow researchers to better control the liquid cell electron microscopy environment, allowing new nanoscale materials science experiments to be conducted systematically in a reproducible manner.

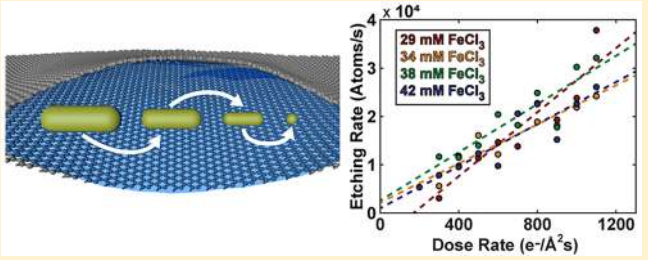

INTRODUCTION

Nanocrystals are an important class of macromolecules that are useful for studying fundamental size-dependent chemical and physical properties,[1−3] and the unique properties that nanocrystals exhibit also open new opportunities in biological,[4−6] catalytic,[7−9] energetic,[10,11] and other applications. Observing the dynamics of nanoscale reactions in their native liquid environment is critical to developing a complete understanding of the mechanisms of these processes. The development of liquid cell electron microscopy has enabled in situ experiments on the length and time scales necessary to capture many nanocrystal chemical transformations.[12−16] Liquid cell electron microscopy experiments on nanocrystal growth,[17−20] etching,[21−24] attachment,[25−27] assembly,[28−30] and other interactions have provided useful information for previously unseen processes. Further advancements such as graphene encapsulation,[26,31−33] heating,[34] and other capabilities in the liquid cell[35] have made liquid cell electron microscopy an even more powerful technique for materials scientists.

For liquid cell electron microscopy to become an integral tool in nanomaterials development, control of the liquid environment for reproducible and systematic experimental design is necessary.[36] The electron beam interacts strongly with the liquid solution being investigated[37,38] and, in the case of water, generates a complex solution of highly reactive radiolysis products.[39−42] The effect of the electron beam on nonaqueous liquids has been less well studied, but the electron beam also affects these solutions as well.[43−45] Although the electron beam greatly affects the composition and resulting chemistry in the liquid cell, it is challenging to make in situ measurements of the concentrations of the radiolysis species during electron microscopy imaging. Simulations have been used to predict the contents of the pockets based on the radiolysis of water,[46,47] but these simulations are more difficult for solutions containing additional species beyond just water itself because reaction rates between many species and the

Received: January 3, 2019
Published: February 19, 2019

DOI: 10.1021/jacs.9b00082
J. Am. Chem. Soc. XXXX, XXX, XXX−XXX

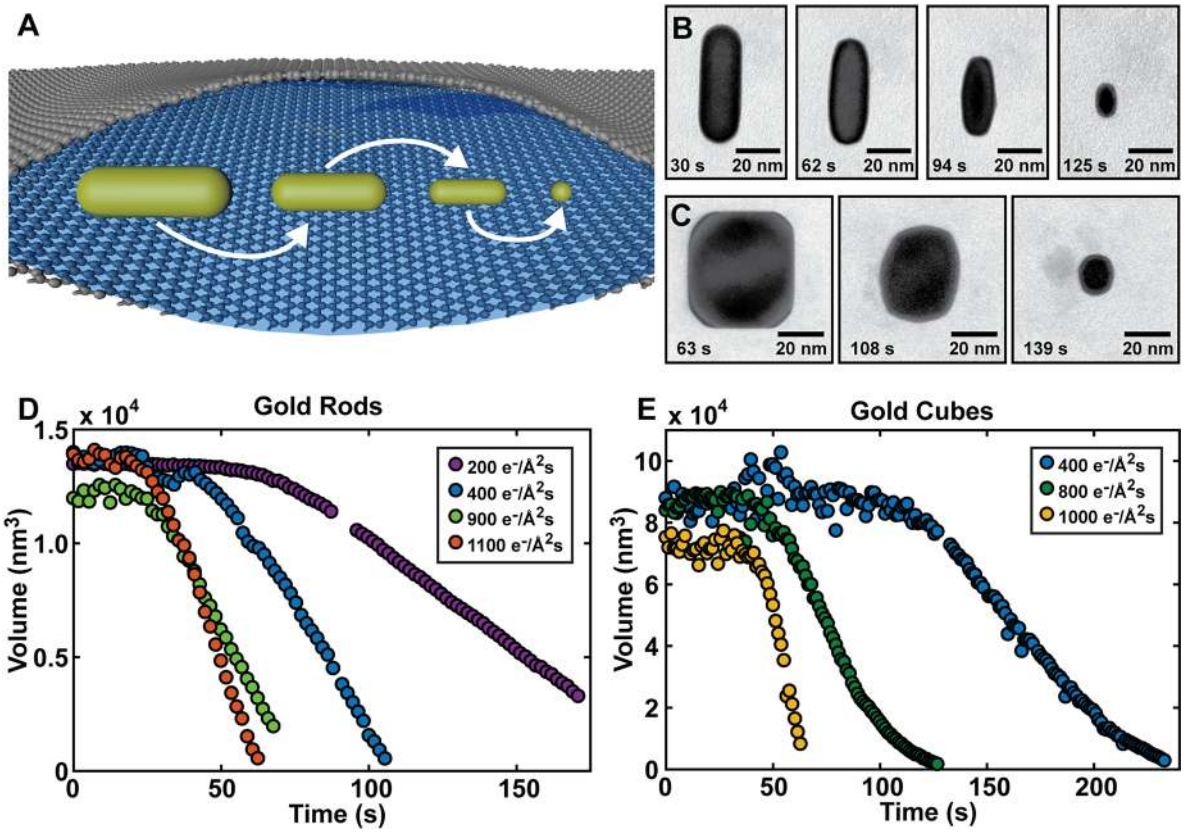

Figure 1. Tracking the volume of gold nanocrystals during etching in the graphene liquid cell. (A) Schematic of the graphene liquid cell. Graphene is used to encapsulate liquid and nanocrystals of interest for imaging during etching using the TEM. (B) Representative individual frames of a gold nanorod undergoing etching. (C) Representative frames of the etching of a gold nanocube. (D) Volume trajectories of the four representative nanorods during etching at different electron beam dose rates. (E) Volume trajectories of three representative nanocubes during etching. For both the nanorods and nanocubes, after an initial period of no etching, the nanocrystals are etched at a constant rate until the end, when they begin to slow down. As the electron beam dose rate increases, the etching rate also increases.

radiolysis products are not known. Instead, a careful study of nanocrystal dynamics as a model system can be used to begin building an understanding of the chemistry occurring in a liquid pocket under electron beam irradiation.[48] Without a better understanding of the chemistry during these in situ experiments, the electron beam can perturb the reactions in unknown ways, making in situ observation difficult to translate to ex situ applications. More importantly, if carefully understood, the radiolysis products can be used as well-defined reagents for promoting desired chemical reactions.

The etching of premade metal nanocrystals[49−52] is an ideal system for determining how to control the chemical contents of a liquid cell due to the large amount of information that can be extracted. Previous work has shown how a combination of preloaded $FeCl_3$ and the beam-induced oxidative radiolysis products can be used to oxidatively etch gold nanocrystals in the graphene liquid cell.[23,53] Using preformed nanocrystals allows the 3D shape of the nanocrystal to be followed during the etching process and parameters such as the volume, shape, and facets to be determined. Tracking of the etching process has already revealed intermediate shapes during etching at high driving forces[23] and the ability to control the facets of these intermediate shapes using the chemical potential of the etchant.[24] In this work, careful analysis of etching trajectories will be used to unravel the chemistry behind how the electron beam and etchant species interact to remove atoms from the nanocrystals.

Following the volume of more than 150 etching particles at varying electron beam dose rates and $FeCl_3$ concentrations reveals the relationship between these two variables and how that controls the etching process. First, hydrogen bubbles are generated while searching for nanoparticles at low dose rates, and these bubbles act as a reservoir of sacrificial reductant that prevents premature etching. Upon raising the electron beam dose rate to the desired etching dose rate, this reservoir of hydrogen bubbles is consumed, and only then does the etching of the nanocrystal commence at a constant rate determined by the electron beam dose rate. The hydrogen bubbles provide a clock for the start of the oxidative etching. The interplay between preloaded $FeCl_3$ and the electron beam dose rate provide two independent methods for tuning the chemical potential and etching rate, respectively. It is hypothesized that the electron beam dose rate sets the combined steady-state concentration of all of the oxidative species in solution and that $FeCl_3$ modulates the relative ratio of those oxidative species. Finally, ex situ work has been done to correlate the in situ TEM experiments with conditions and reactants traditionally used during nanocrystal syntheses. Through an understanding of how to use the electron beam and reactants to control the chemistry of oxidative etching in the liquid cell, future experiments will be able to be systematically performed and more easily translated to bulk colloidal syntheses.

DOI: 10.1021/jacs.9b00082
J. Am. Chem. Soc. XXXX, XXX, XXX−XXX

METHODS

Nanocrystal Synthesis. Synthesis followed previous literature precedent.[54,55] All water used was filtered with a Millipore water filter.

Gold Nanorods. $HAuCl_4$ (10 mM, 125 μL, Sigma-Aldrich) was mixed with 5 mL of 100 mM hexadecyltrimethylammonium bromide (CTAB, TCI) before adding 300 μL of 10 mM ice-cold $NaBH_4$ (Sigma-Aldrich). After stirring for 1 min, the solution was aged for 30 min. This solution (24 μL) was injected into 20 mL of 100 mM CTAB, 1 mL of 10 mM $HAuCl_4$, 0.18 mL of 10 mM $AgNO_3$ (Sigma-Aldrich), and 0.114 mL of 100 mM ascorbic acid (Sigma-Aldrich). This nanorod solution was centrifuged two times for 15 min at 8000 rpm.

Gold Nanocubes. After redispersing the gold nanorods in 50 mM CTAB, the optical density, OD, of the LSPR was brought to 2. Between 0.087 and 0.105 μL of 1 mM $HAuCl_4$, depending on the size of the rods, was added for each milliliter of nanorod solution and was stirred gently for 4 h at 40 °C. The solution of spherical seeds was centrifuged two times for 30 min at 11 000 rpm and brought to an OD of 1 with 100 mM cetylpyridinium chloride (CPC, TCI). Between 350 and 400 μL of spherical seeds, depending on the desired size, was injected into a solution of 5 mL of 100 mM CPC, 500 μL of 100 mM KBr, 100 μL of 10 mM $HAuCl_4$, and 150 μL of 100 mM ascorbic acid.

Gold Rhombic Dodecahedra. Between 50 and 100 μL of spherical seeds, depending on the desired size, was injected into a solution of 5 mL of 100 mM CPC (TCI), 250 μL of 1 M HCl (Fisher Chemical), 13 μL of 10 mM $AgNO_3$, 250 μL of 10 mM $HAuCl_4$, and 30 μL of 100 mM ascorbic acid.

Graphene Liquid Cell Fabrication. Graphene liquid cells were fabricated following a reported procedure.[53] Graphene (3−5 layers, ACS materials) was transferred onto holey amorphous carbon, gold quantifoil TEM grids (SPI Supplies, 300 mesh, R1.2/1.3), and these grids were used to encapsulate a solution of 104 mM $FeCl_3$ (Sigma-Aldrich) in 22 mM HCl (Fisher Chemical), 100 mM tris-(hydroxymethyl)aminomethane hydrochloride, Tris-HCl, (Fisher Biotech), and the nanocrystals of interest. The volumes of $FeCl_3$/HCl and Tris-HCl were modulated to yield the desired final $FeCl_3$ concentration. All videos were taken between 30 min and 3 h after encapsulation.

TEM Imaging Conditions. All TEM imaging was performed on a FEI Tecnai T20 S-Twin TEM operating at 200 kV with a LaB_6 filament. A time series of TEM images was collected with a Gatan Orius SC200 camera using a custom digital micrograph script with a full 2048 × 2048 readout with a binning of 2 pixels in each direction at a nominal magnification of 71K×, resulting in a pixel resolution of 1.5 Å/pixel. The exposure time was 0.5 s with a readout time of 0.8 s, yielding a frame rate of 0.77 fps. For the TEM electron beam dose rate calibration script (further details in S1), a conversion value of 6.7 was used to convert CCD counts to electrons. There may be a systematic inaccuracy based on this conversion value; however, all of the data is self-consistent, and the conclusions drawn are based on trends in the data and thus are independent of the exact conversion value.

RESULTS AND DISCUSSION

In these liquid cell transmission electron microscopy (TEM) experiments, premade gold nanocrystals are added to an aqueous solution of $FeCl_3$ and Tris-HCl, and the solution is encapsulated between graphene sheets for imaging in the TEM.[53] The concentrations of $FeCl_3$ are low enough that the gold nanocrystals do not begin to be etched until electron beam irradiation reaches a sufficiently high dose rate. Through a combination of the preloaded $FeCl_3$ and beam-induced radiolysis species, the nanocrystals undergo oxidative etching and the nanocrystals' etching trajectories can be observed (Figure 1A). In this high-driving-force etching regime, gold nanorods (Figure 1B) maintain their aspect ratio while gold cubes (Figure 1C) and rhombic dodecahedra encompassed by {100} and {110} facets take on an intermediate tetrahexahedral shape with {hk0} facets.[23,24] Because the shape and orientation of the preformed gold nanocrystals is known, the 3D shape of the nanocrystals can be inferred from the 2D pictures of the nanocrystal in each frame of the etching movie (Figure S3). The 3D shape of the nanocrystals during each step in the etching trajectory provides information about the kinetics of this reaction and the underlying chemistry that is occurring in the complex environment of the graphene liquid cell.

Regardless of the initial shape of the gold nanocrystal being etched, the volume trajectories are remarkably similar. Upon irradiation of both the gold nanorods (Figure 1D) and gold nanocubes (Figure 1E) at the desired etching electron beam dose rate, there is initially an induction period with no volume change before etching of the nanocrystals at a constant rate. When the nanocrystals become small, the etching rate slows down. This similar type of trajectory can also be observed for the oxidative etching of rhombic dodecahedra (Figure S4). Using a home-written Digital Micrograph script to calibrate and control the condenser system of the TEM, the electron dose rate was reproducibly modulated to investigate the effect of the dose rate on the etching rate. (See the Supporting Information for the script outline.) As the dose rate increases for nanocrystals in pockets of otherwise identical experimental conditions, the etching rate also becomes faster in a linear proportion. The increase in the electron dose rate is believed to cause an increase in the concentration of oxidative beam-generated species that are etching the nanocrystals.[48] By etching numerous nanocrystals while adjusting the dose rate and $FeCl_3$ concentration, the chemistry of the liquid cell environment can be better understood to explain the occurrence of the induction period, the constant etching rate, and the decrease in etching rate at small nanocrystal sizes.

To provide enough data for a meaningful study of the kinetics of this etching process, more than 150 individual etching trajectories were collected and analyzed. Not every nanocrystal was successfully etched to completion because of a couple of identifiable failure modes, and these trajectories were not used in the analysis (Figure S7). Roughly 8% of graphene liquid cell pockets dried out during the etching of a nanocrystal, leading to a rapid decrease in the etching rate until the particle stopped etching, often accompanied by a lack of bubbles. Etching that slowed or stopped provided a quantifiable metric for determining when an etching trajectory was no longer providing useful data; however, on the basis of the contrast of the liquid in the pocket, most pockets did not lose liquid during the imaging process (Figure S8). The other factor that occasionally disrupted the etching trajectories was the precipitation of iron oxyhydroxide around the etching nanocrystal. Small particles that formed in solution and did not seem to affect the etching were determined to be FeO(OH) from HRTEM.[56,57] (Figure S9) In some videos, a more perturbative, halolike feature emerges around the nanocrystal, and from HRTEM, it was determined to be Fe-$(OH)_3(H_2O)_{0.25}$[56,58] (Figure S10). When this iron oxyhydroxide grows on or close to the surface of the etching nanocrystal, the precipitate limits the etchant species from getting to the nanocrystal surface and causes a slower, but still constant, etching rate (Figure S12). This slowed etching rate, which occurred in roughly 20% of the trajectories, seems to be diffusion-limited because the etchant species has to travel through a penumbra of precipitated iron oxyhydroxide, and

DOI: 10.1021/jacs.9b00082
J. Am. Chem. Soc. XXXX, XXX, XXX−XXX

these slow trajectories were also not used in the analysis of the effect of $FeCl_3$ concentration and electron beam dose rate on the kinetics of etching. The formation of these iron oxyhydroxides is unsurprising because of the presence of the hydroxide radical and other highly oxidative species in the liquid cell pockets. This precipitation did not affect a significant number of etching trajectories and seemed to be suppressed when the initial nanocrystal solution had less residual surfactant. Although this precipitation was undesirable, it did show the advantage of using a thin encapsulation material such as graphene to be able to see the lattice fringes of solid species in solution.

The beginning of the etching trajectories has an induction period with no observable removal of atoms from the nanocrystals, and this delay is a useful feature that enables the entire etching trajectory to be viewed while also revealing important insights into the chemistry of the liquid pockets. The process of imaging the nanocrystals first involves searching for and focusing on nanocrystals in liquid pockets. This searching process is performed at relatively low electron beam dose rates (around 20 to 40 $e^-/Å^2$ s) to prevent etching before video collection has started. After a nanocrystal is properly in focus, the video collection is started while simultaneously increasing the electron beam dose rate to between 300 and 1300 $e^-/Å^2$ s through an automated microscope control and data collection script. This is considered to be time zero for the etching trajectories. At time zero, nanobubbles are observed in solution, congregated around the nanocrystals. As the electron beam illumination continues, the bubbles shrink with no observable etching of the nanocrystals (Figure 2A). After all of the bubbles have been consumed, atoms abruptly begin being removed from the gold nanocrystals. These nanobubbles that appear to be protecting the nanocrystals are rapidly generated while illuminating the liquid pocket at low electron beam dose rates (Figure 2B). This protection of the nanocrystals is extremely useful because it prevents etching of the nanocrystals before the imaging has started, providing a reproducible starting point for each trajectory.

A combination of oxidation chemistry and the literature on liquid cell electron microscopy experiments can be used to explain the chemistry involved in the nanobubbles acting as a sacrificial reductant preventing the gold nanocrystals from initially etching. For now, these sorts of indirect methods are needed to determine how the added $FeCl_3$ and Tris-HCl cause the observed behavior because an exact measurement of the concentrations of chemical species in solution is not within our current experimental capabilities. Radiolysis of the water solution in the liquid cell rapidly produces a steady-state amount of hydrogen gas,[16,37,40,46,59] and because the sacrificial nanobubbles in these etching experiments appear only upon beam illumination, it is reasonable to identify these nanobubbles as hydrogen gas. The bubbles are not likely to be thermally generated because the temperature rise in the liquid cell is predicted to be only a few °C, which would not be enough to boil the water.[59,60] Upon increasing the electron beam dose rate by an order of magnitude, it is hypothesized that more oxidative radical species are generated, and these additional oxidative species first consume the bubbles before etching the gold nanocrystal. Using kinetic models of the radiolysis products in water under the TEM conditions in this experiment,[46] the concentration difference between oxidative species such as hydrogen peroxide and hydroxide radical and reductive species such as the hydrated electron and hydrogen

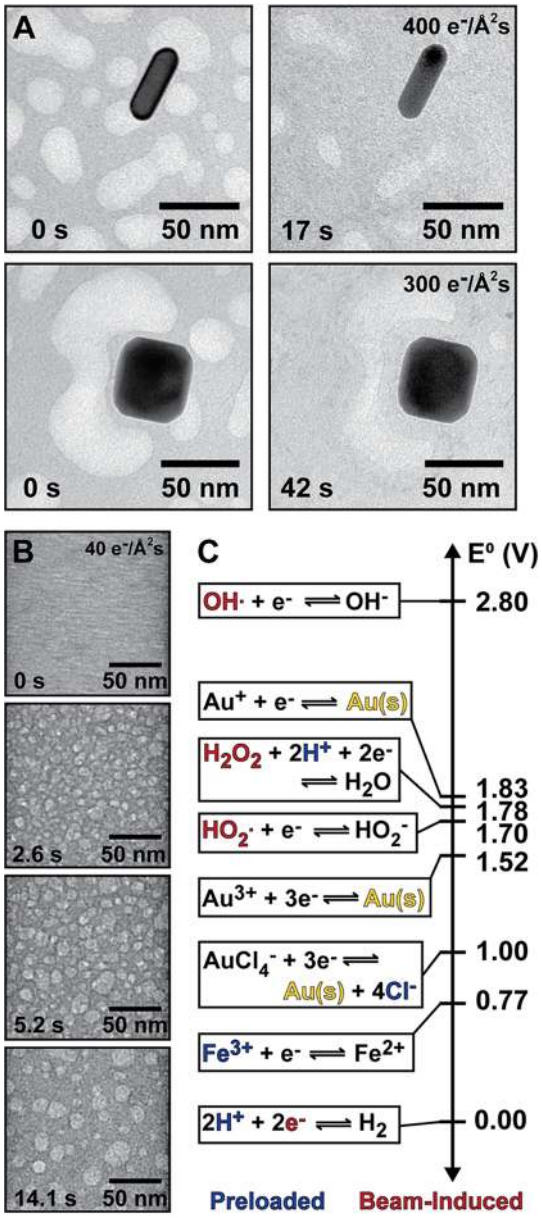

Figure 2. Hydrogen bubbles generated at low dose rates cause an initial induction period. (A) Representative images showing hydrogen bubbles around the nanocrystals. While searching for nanocrystals in the pockets at low electron dose rates, hydrogen bubbles are generated. After increasing the dose rate for etching, hydrogen bubbles are consumed first before etching of the nanocrystals can begin. (B) Images showing the generation of bubbles when the liquid is irradiated at a low dose rate of 40 $e^-/Å^2$s. (C) Oxidation potentials of the beam-generated species, preloaded species, and gold species in volts under standard conditions.[47−51]

radical increases as the electron dose rate increases[47] (Figure S13). Looking at the reduction potentials of the relevant species in solution, the beam-generated oxidative species of the OH radical, H_2O_2, and HO_2 radical have the strongest affinity for an electron[61−65] (Figure 2C). Among the gold nanocrystals, iron ions, and hydrogen bubbles in solution, the hydrogen bubbles are most readily oxidized. In this way, the hydrogen bubbles that are generated at low electron beam dose rates could act as a sacrificial species that can be oxidized before the nanocrystals undergo oxidative etching.

DOI: 10.1021/jacs.9b00082
J. Am. Chem. Soc. XXXX, XXX, XXX−XXX

The nanobubbles also provide insight into the physical structure of the liquid cell pocket. The observation of more bubbles at low dose rates is a little unexpected because of reports in the literature of more bubble generation at higher electron beam dose rates,[60,66] but the difference in preloaded species and the oxidative nature of this liquid environment are likely responsible for this difference. Once the hydrogen bubbles begin forming at low electron dose rates, they rapidly coalesce into larger, steady bubbles (Figure S14). The bubbles congregate around the large cubic nanocrystals, indicating that cubic nanocrystals may be causing the liquid pockets to bulge outward. The smaller nanorods have less congregation of bubbles around them, which also suggests that the height of the liquid pockets is closer in size to the 50−60 nm cubes. It is important to note that nanocubes are uniformly etched at a constant rate, so the graphene likely is not tightly wrapping the gold nanocubes. Wrapping the particles tightly would involve pushing out the last few nanometers of liquid between the particle and the graphene, and previous work has shown that squeezing out these small layers of water between two surfaces is very difficult.[67,68] After the hydrogen bubbles are consumed by the oxidative species in solution, other bubbles can sometimes be seen coming from outside the viewing area toward the nanoparticle before eventually being consumed. The bubbles never go over the nanocubes but rather rotate around them in a remarkedly consistent pattern, further indicating that the height of the pockets is not significantly larger than the nanocubes' size (Figure S15). It is unexpected to see the movement of bubbles toward the center of the electron beam illumination, especially with the visible diffusion of gold ions away from the etching nanocrystal. Possibly, the bulge in the pocket caused by the particle is drawing the bubbles in toward the center. Although there are numerous studies of nanoscale bubbles using liquid cell electron microscopy,[59,60,69−71] future studies could potentially use this setup to investigate how nanoscale bubbles move in a current or when a driving force is applied. Unlike previous nanomaterials studies where beam-generated bubbles were an undesirable nuisance,[18,38,72] these etching experiments use the beam-generated hydrogen bubbles as a sacrificial reductant timer for better data collection.

After the bubbles are consumed, etching of the nanocrystals rapidly reaches a steady rate of atom removal, and the effect of the electron beam dose rate and $FeCl_3$ concentration on the etching rate provides valuable insight into the chemistry of the liquid pocket. For each graphene liquid cell loaded with a known initial $FeCl_3$ concentration, multiple nanocrystals can be etched over a range of electron beam dose rates using the automated, home-written TEM script. In Figure 3A,B, etching rates at different dose rates are shown for nanorods and nanocubes, respectively. The colors represent different initial $FeCl_3$ concentrations, and each data point for the nanorods represents the average of multiple etching trials under those conditions. (See Figure S17 for a plot of rod etching rates including uncertainty bars.) The data for the nanocubes has more scatter because it was more difficult to acquire multiple trajectories for each dose rate for averaging. The etching rate varies linearly with the electron beam dose rate for both the nanorods and nanocubes, indicating that the oxidative species generated by the electron beam are the limiting reagents in this reaction. The cubes have a steeper slope for the linear fits because the far larger size of the cubes allows the cubes to interact with a greater number of oxidative species over a larger area of the liquid pocket. Conversely, there is no measurable change in the etching rate as the initial $FeCl_3$ concentration is varied, at least within our current measurement precision. Although the range of $FeCl_3$ concentrations is not large, previous work has shown that the potential of the liquid cell environment and the subsequent facets that are formed on the intermediate shapes are noticeably different over this range of initial $FeCl_3$ concentrations.[24] Because the $FeCl_3$ concentration controls only the chemical potential and the electron beam dose rate controls only the rate of etching (Figure S18), the potential and etching rate can be independently controlled to

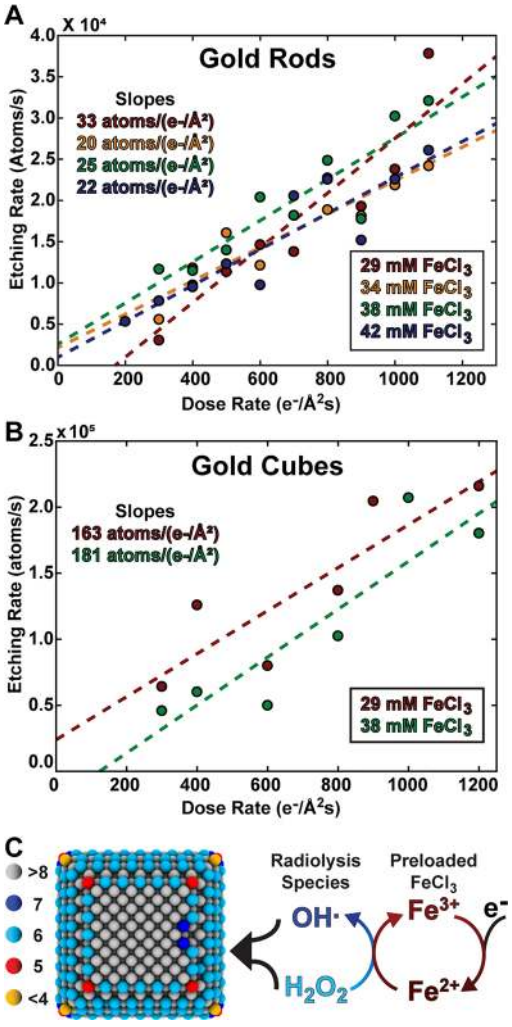

Figure 3. Etching rate dependence on the electron beam dose rate. (A) The etching rate of gold nanorods scales linearly with the dose rate, but the initial $FeCl_3$ concentration has a negligible effect on the etching rate. Each data point is the average of multiple nanocrystal etchings at that dose rate and $FeCl_3$ concentration. (B) Etching rate of gold nanocubes as a function of dose rate and initial $FeCl_3$ concentration. The data has more scatter because fewer trajectories were able to be attained at each dose rate, but the etching rate still scales relatively linearly with the dose rate. (C) Model for how the electron beam dose rate determines the etching rate and how the $FeCl_3$ concentration controls the chemical potential of etching. Looking at the nanocube on an atomic level, the edges are made up of six- and seven-coordinate atoms. It is proposed that only the electron-beam-generated oxidative species can remove these atoms, and the concentration of these oxidative species in solution is determined by the beam dose rate. $FeCl_3$ controls the ratios of these oxidative species, determining the potential of the oxidative environment.

DOI: 10.1021/jacs.9b00082
J. Am. Chem. Soc. XXXX, XXX, XXX−XXX

provide researchers systematic control over etching reactions in the graphene liquid cell.

The independent nature of the control over the etching rate and chemical potential yields insight into the chemical reactions occurring in these etching studies. Because the beam-generated oxidative species are far more oxidative than the Fe(III) ions (Figure 2C), it seems most probable that beam-generated species such as hydroxide radicals and hydrogen peroxide are actively oxidizing the gold atoms on the surface of the nanocrystal. Because the electron beam dose rate should control the concentration of beam-generated species in solution, the hypothesis that beam-generated species are actively etching the nanocrystal is consistent with the observation that increasing the beam dose rate increases the etching rate. Although the electron beam controls the total quantity of etching species in solution, the etching species do not all have the same etching strength. For example, the hydroxide radical is far more oxidative than hydrogen peroxide. Because $FeCl_3$ has previously been shown to control the oxidative potential of the environment, we propose that instead of directly removing gold atoms, the $FeCl_3$ modulates the ratio between the oxidative species generated by the electron beam. The more $FeCl_3$ that is added to the liquid cell, the greater the ratio of the stronger oxidative species such as the hydroxide radical to the slightly weaker oxidative species such as hydrogen peroxide. This model allows the electron beam dose rate to control the rate of atom removal by controlling the total concentration of etching species in solution and allows the $FeCl_3$ concentration to modulate the potential by deciding the ratio between individual beam-generated species.

The chemistry of the liquid cell is a complex mixture of interrelated chemical reactions and equilibria that lead to a steady state, so it is difficult to definitively claim that one reaction or pathway allows $FeCl_3$ to modulate the radical concentrations. Ideally, we would measure the concentrations of the radical species in the liquid cell pocket under different reaction conditions, but we currently do not have the experimental capabilities in our TEM to do those experiments. However, we consider here an example of a simple hypothesis that appears to be plausible. The ability of iron ions to react with hydrogen peroxide to yield the hydroxide radical is not unprecedented in the literature. The initial Fe(III) ions likely react quickly with the hydrated electrons, yielding Fe(II) ions.[73] These Fe(II) ions could react with hydrogen peroxide through the well-studied Fenton reaction to yield Fe(III), OH−, and the hydroxide radical.[74−76] This process would be cyclic, both removing reductive aqueous electrons from solution and converting hydrogen peroxide to the more oxidative hydroxide radical without changing the total number of oxidative species in solution (Figure 3C). This pathway could be but one piece of a larger assortment of chemical processes that lead to a steady state of species in the liquid cell, but the hypothesis that $FeCl_3$ can modulate the ratios of oxidative species is well within literature precedent, especially in an acidic environment such as our liquid solution.[73,77,78]

Although all of the etching nanocrystals have a constant etching rate for the majority of their etching trajectory, the etching rate often slows down as the nanocrystals become small. This deviation can be clearly seen when overlaying the measured volume of the etching cubes (Figure 4A) and nanorods (Figure 4B) on the linear fits to the constant etching region. For the majority of the etching trajectory, the measured volumes lie directly on the linear best fit; however, each

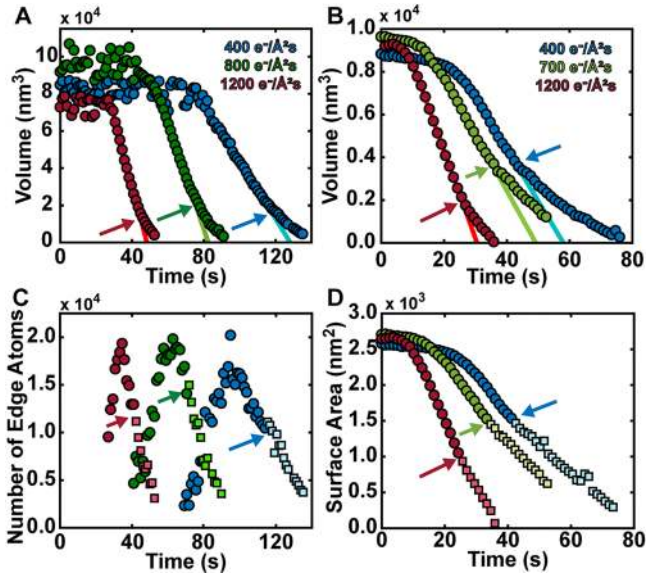

Figure 4. Slowing of the etching rate at the end of the trajectories. (A) Volume of etching gold nanocubes on top of the linear fits. Arrows show where the volumes begin to deviate from the linear fits. (B) Volumes of etching gold nanorods on top of linear fits. Arrows show where the volumes begin to deviate from the linear fits. (C) Estimated number of edge sites for each frame in the etching cube videos. Circles are the constant etching rate region, and cubes are the slowed etching region. Arrows show the crossover point. (D) Surface area of etching gold nanorods, with circles being the linear etching region and squares being the slowed etching region. Arrows show the crossover point.

volume trajectory begins deviating from the linear fit at the points labeled by the arrows. Because this deviation consistently happens at the end of the etching trajectory independently of the total etching time, it is unlikely that this declining etching rate is caused by a drying pocket or other defects in the liquid cell. A more reasonable hypothesis is that this slowing of the etching rate as the particles become small corresponds to a change in the limiting reactant from the number of beam-induced oxidative species in solution to the number of edge sites on the nanocrystals. Because only the surface atoms can be etched, the rate at which atoms can be removed when the nanocrystal is small could be limited by the number of exposed atoms. The number of edge atoms on the cube, which because of their small number of bonds are the most likely atoms to be etched, can be estimated using the volumes and facets from each frame of the etching video (Figure 4C). Initially, the number of edge sites increases as the nanocrystal transforms from a {100} cube to an {*hk*0} tetrahexahedral shape, but eventually the decrease in size leads to a decrease in the number of edge sites. The point where the volume deviates from the linear fit is marked with arrows. For the nanorods, the number of edge sites cannot be estimated because the facets on the nanorod are not fully known, but the surface area of the rods is a reasonable proxy for the number of removable surface atoms on the nanocrystal (Figure 4D). The surface area decreases during the etching, and the deviation point in the volume trajectories is shown with an arrow. Investigating how the deviation point changes with the electron beam dose rate and with the $FeCl_3$ concentration could provide more information about these etching reactions, but more trajectories with obvious crossover

DOI: 10.1021/jacs.9b00082
J. Am. Chem. Soc. XXXX, XXX, XXX−XXX

points are needed to provide clearer conclusions about the effects of these parameters (Figure S19). The change in the limiting reactant seems like a reasonable hypothesis for the observed behavior and could be an interesting area to explore further with in situ electron microscopy.

These liquid cell TEM experiments provide a wealth of information on the mechanisms of oxidative etching of gold nanocrystals, but ultimately, these in situ experiments are useful only if the information learned can be correlated and applied to ex situ syntheses. Because the longitudinal surface plasmon resonance (LSPR) of gold nanorods depends strongly on the nanorod aspect ratio (ratio between the length and width of the nanorod) and the absorption cross section at a given LSPR wavelength is determined by the size of the nanorod, the size and shape of the gold nanorods can be followed by taking extinction spectra during the oxidative etching process.[79] Although this is a bulk technique that can no longer follow subtle shape or facet changes during the etching process, the extinction spectra provide a tool for comparing the experimental conditions in the liquid cell with traditional colloidal synthesis conditions. In addition, these correlative studies show that the processes seen in the liquid cell are not simply byproducts of liquid cell electron microscopy.

Reproducing the oxidative etching seen in the graphene liquid cell required control of the ex situ etching kinetics. Previous work oxidatively etching gold nanorods has shown the ability to etch nanorods from the tips, thereby decreasing the aspect ratio and leading to a blue shift in the LSPR during the etching process.[79,80] Because the etching proceeds by removing only the lowest coordinated atoms from the tips of the nanorod, this method of etching will be called the low-driving-force regime (Figure 5A). For nanorod etching experiments in the graphene liquid cell, the rods did not just etch from the tips but rather the aspect ratio stayed relatively constant until the end of the trajectory (Figure S20). This high-driving-force etching showed a decrease in both the length and width during the etching process.[23] To control the ex situ etching between the high-driving-force and low-driving-force regimes, the concentration of the $FeCl_3$ oxidative etchant was modulated. By taking the same nanorod sample and increasing the $FeCl_3$ concentration an order of magnitude from 0.135 to 1 M, the gold rods were controllably etched in the low-driving-force and high-driving-force regimes, respectively (Figure 5B,C)

With the ability to reproduce in a colloidal solution the reactions seen in the graphene liquid cell, comparisons can be made between the two environments. In the liquid cell, it is proposed that $FeCl_3$ does not directly oxidize the nanorods as a result of the much greater oxidizing power of the beam-induced species, and this is consistent with the observation that a solution with 40 mM $FeCl_3$ and the same contents as a liquid cell takes hours for noticeable etching (Figure S22). High-driving-force etching of the nanorods using simply $FeCl_3$ requires a concentration 25 times greater than what was used in the liquid cell. In addition, the in situ observation that changing the $FeCl_3$ concentration over the range of 29 to 42 mM showed no measurable change in the etching rate is consistent with ex situ measurements of the etching rate that confirm that the etching rate change would have been below the measurement threshold (Figure S23). This high-driving-force etching provides an avenue for making energetically unfavorable shapes, and ultimately the goal would be to use this technique to synthesize large numbers of these shapes

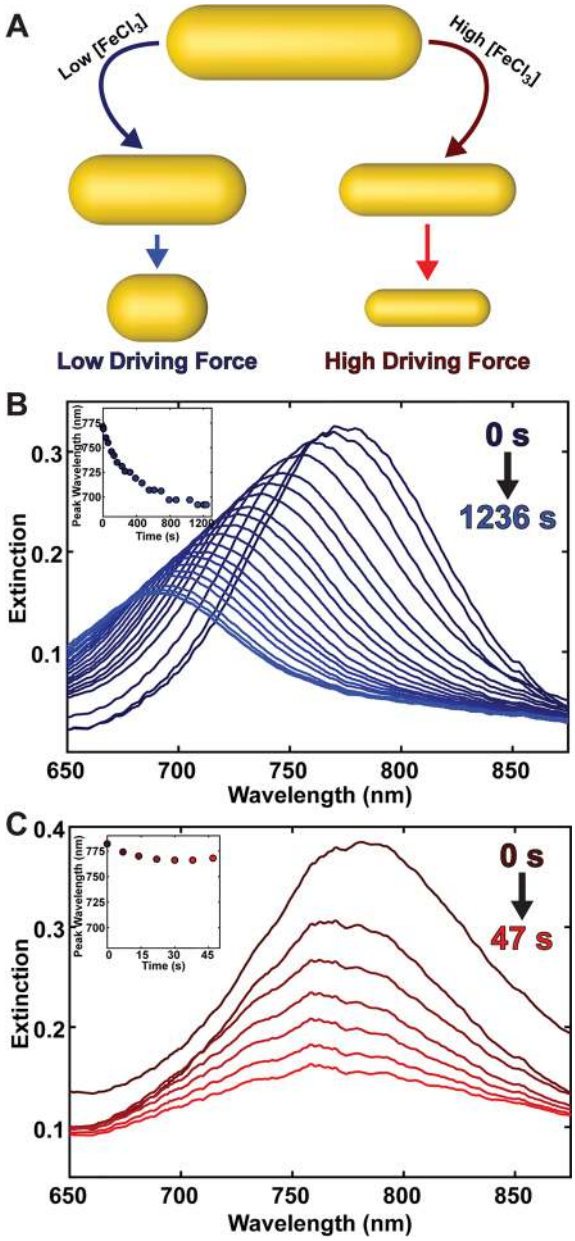

Figure 5. Ex situ low-driving-force and high-driving-force oxidative etching of gold nanorods. (A) Schematic of low-driving-force etching from the tips of the nanorod and high-driving-force etching maintaining the aspect ratio. (B) Extinction spectra while etching in a low-driving-force regime. The inset shows the LSPR blue shifting during etching. (C) Extinction spectra while etching in a high-driving-force regime. The inset shows the LSPR staying relatively constant.

using colloidal chemistry. Unfortunately, stopping the etching reaction and locking in the shape has proven difficult as the nanocrystals rearrange from their kinetic shape. This rearrangement is consistent with liquid cell TEM observations of nanocubes that stop etching to a {*hk*0} tetrahexahedron due to a drying of the pocket and relax back to a nanocube with lower-energy facets (Figure S24). This rearrangement is further evidence for the need to view nanocrystal reactions in situ rather than by quenching the reaction at different times and then looking at the sample. Potentially, by adding tighter-binding ligands after the high-driving-force etching or quenching them at low temperatures to stop surface diffusion, the oxidative etching mechanisms seen in the liquid cell will be

DOI: 10.1021/jacs.9b00082
J. Am. Chem. Soc. XXXX, XXX, XXX−XXX

harnessed to control the nonequilibrium facets on colloidal gold nanocrystals.

Understanding, and ultimately controlling, the chemistry during liquid cell electron microscopy experiments is vital to making the results applicable for purposes outside of the electron microscope. The electron beam and radiolysis species generated by the electron beam are an undeniable factor in liquid cell electron microscopy experiments that must be accounted for, but this presumed limitation can be mitigated or turned into an advantage as researchers continue to better understand the chemistry taking place. Through the reproducible oxidative etching of gold nanocrystals, a deeper understanding of the liquid cell environment was gained, and the ability to independently control the etching rate and chemical potential was achieved. The exact chemistry of each liquid cell electron microscopy experiment may be slightly different depending on the additives, solvent, and encapsulation technique, but using the electron beam dose rate to control the unfolding sequence of events during the observation of a sample should be transferable. In addition, the idea of using activation processes such as the Fenton reaction to modulate the chemical species in the liquid cell should provide a foundation for developing other liquid systems to study a variety of other nanoscale reactions and dynamics. Correlated ex situ experiments are also critical in liquid cell electron microscopy development for both understanding the chemistry and providing evidence that results in the liquid cell are not simply a product of the liquid cell environment. For liquid cell electron microscopy to truly make a tangible difference in the materials science community, the insights need to lead to improved synthesis methods or other advances outside the electron microscope, and the continued understanding of the chemistry in the graphene liquid cell will make the technique even more widely applicable in the future.

■ ASSOCIATED CONTENT

Supporting Information

TThe Supporting Information is available free of charge on the ACS Publications website at DOI: 10.1021/jacs.9b00082.

Au nanorod etching in 34 mM $FeCl_3$ at a dose rate of 400 $e^-/Å^2$ s (AVI)

Au nanorod etching in 34 mM $FeCl_3$ at a dose rate of 800 $e^-/Å^2$ s (AVI)

Au nanorod etching in 34 mM $FeCl_3$ at a dose rate of 1200 $e^-/Å^2$ s (AVI)

Au nanorod etching in 38 mM $FeCl_3$ at a dose rate of 400 $e^-/Å^2$ s (AVI)

Au nanorod etching in 38 mM $FeCl_3$ at a dose rate of 800 $e^-/Å^2$ s (AVI)

Au nanorod etching in 38 mM $FeCl_3$ at a dose rate of 1200 $e^-/Å^2$ s (AVI)

Au cube etching in 29 mM $FeCl_3$ at a dose rate of 400 $e^-/Å^2$ s (AVI)

Au cube etching in 29 mM $FeCl_3$ at a dose rate of 800 $e^-/Å^2$ s (AVI)

Au cube etching in 29 mM $FeCl_3$ at a dose rate of 1200 $e^-/Å^2$ s (AVI)

Au cube etching in 38 mM $FeCl_3$ at a dose rate of 400 $e^-/Å^2$ s (AVI)

Au cube etching in 38 mM $FeCl_3$ at a dose rate of 800 $e^-/Å^2$ s (AVI)

Au cube etching in 38 mM $FeCl_3$ at a dose rate of 1200 $e^-/Å^2$ s (AVI)

EM dose rate control script, rhombic dodecahedra etching trajectory, beam and pocket stability, precipitating iron oxyhydroxide species, kinetic models of chemical components, bubble movement, uncertainty bars on etching rate plots, effect of dose rate on facet and crossover points, aspect ratio change during nanorod etching, ex situ rod etching extinction spectra and TEM characterization, and relaxation of etching nanocube facets when a pocket dries out (PDF)

■ AUTHOR INFORMATION

Corresponding Author

*paul.alivisatos@berkeley.edu

ORCID

Matthew R. Hauwiller: 0000-0002-5448-6937

Justin C. Ondry: 0000-0001-9113-3420

A. Paul Alivisatos: 0000-0001-6895-9048

Notes

The authors declare no competing financial interest.

■ ACKNOWLEDGMENTS

The work was supported by the U.S. Department of Energy, Office of Science, Office of Basic Energy Sciences, Materials Sciences and Engineering Division under contract no. DE-AC02-05-CH11231 within the Physical Chemistry of Inorganic Nanostructures Program (KC3103). C.M.C. acknowledges the UC Berkeley SMART program for summer research funding. Prof. Matt Jones is acknowledged for his useful conversations, and Vishnu Dharmaraj is acknowledged for his synthesis help. The authors also acknowledge Negest Williams for her invaluable administrative support. The raw TEM data presented are available on the DASH repository at DOI 10.6078/D17T13, 10.6078/D1N387, 10.6078/D1H97P, and 10.6078/D1CM2N.

■ REFERENCES

(1) Buffat, P.; Borel, J.-P. Size Effect on the Melting Temperature of Gold Particles. *Phys. Rev. A: At., Mol., Opt. Phys.* **1976**, *13* (6), 2287–2298.

(2) Ondry, J. C.; Hauwiller, M. R.; Alivisatos, A. P. Dynamics and Removal Pathway of Edge Dislocations in Imperfectly Attached PbTe Nanocrystal Pairs: Toward Design Rules for Oriented Attachment. *ACS Nano* **2018**, *12* (4), 3178–3189.

(3) Alivisatos, A. P. Perspectives on the Physical Chemistry of Semiconductor Nanocrystals. *J. Phys. Chem.* **1996**, *100* (31), 13226–13239.

(4) Huang, X.; El-Sayed, I. H.; Qian, W.; El-Sayed, M. A. Cancer Cell Imaging and Photothermal Therapy in the Near-Infrared Region by Using Gold Nanorods. *J. Am. Chem. Soc.* **2006**, *128* (6), 2115–2120.

(5) Huang, X.; El-Sayed, M. A. Plasmonic Photo-Thermal Therapy (PPTT). *Alexandria J. Med.* **2011**, *47* (1), 1–9.

(6) Khosla, K.; Wang, Y.; Hagedorn, M.; Qin, Z.; Bischof, J. Gold Nanorod Induced Warming of Embryos from the Cryogenic State Enhances Viability. *ACS Nano* **2017**, *11* (8), 7869–7878.

(7) You, H.; Yang, S.; Ding, B.; Yang, H. Synthesis of Colloidal Metal and Metal Alloy Nanoparticles for Electrochemical Energy Applications. *Chem. Soc. Rev.* **2013**, *42* (7), 2880–2904.

DOI: 10.1021/jacs.9b00082
J. Am. Chem. Soc. XXXX, XXX, XXX–XXX

(8) Jing, H.; Zhang, Q.; Large, N.; Yu, C.; Blom, D. A.; Nordlander, P.; Wang, H. Tunable Plasmonic Nanoparticles with Catalytically Active High-Index Facets. *Nano Lett.* **2014**, *14* (6), 3674−3682.
(9) Wu, B.; Zheng, N. Surface and Interface Control of Noble Metal Nanocrystals for Catalytic and Electrocatalytic Applications. *Nano Today* **2013**, *8* (2), 168−197.
(10) Talapin, D. V.; Lee, J.-S.; Kovalenko, M. V.; Shevchenko, E. V. Prospects of Colloidal Nanocrystals for Electronic and Optoelectronic Applications. *Chem. Rev.* **2010**, *110* (1), 389−458.
(11) Lu, X.; Rycenga, M.; Skrabalak, S. E.; Wiley, B.; Xia, Y. Chemical Synthesis of Novel Plasmonic Nanoparticles. *Annu. Rev. Phys. Chem.* **2009**, *60* (1), 167−192.
(12) Williamson, M. J.; Tromp, R. M.; Vereecken, P. M.; Hull, R.; Ross, F. M. Dynamic Microscopy of Nanoscale Cluster Growth at the Solid−liquid Interface. *Nat. Mater.* **2003**, *2* (8), 532−536.
(13) Radisic, A.; Ross, F. M.; Searson, P. C. In Situ Study of the Growth Kinetics of Individual Island Electrodeposition of Copper. *J. Phys. Chem. B* **2006**, *110* (15), 7862−7868.
(14) de Jonge, N.; Ross, F. M. Electron Microscopy of Specimens in Liquid. *Nat. Nanotechnol.* **2011**, *6* (11), 695−704.
(15) Zheng, H.; Smith, R. K.; Jun, Y. -w.; Kisielowski, C.; Dahmen, U.; Alivisatos, A. P. Observation of Single Colloidal Platinum Nanocrystal Growth Trajectories. *Science* **2009**, *324* (5932), 1309−1312.
(16) Ross, F. M. Opportunities and Challenges in Liquid Cell Electron Microscopy. *Science* **2015**, *350* (6267), aaa9886.
(17) Ahmad, N.; Wang, G.; Nelayah, J.; Ricolleau, C.; Alloyeau, D. Exploring the Formation of Symmetric Gold Nanostars by Liquid-Cell Transmission Electron Microscopy. *Nano Lett.* **2017**, *17* (7), 4194−4201.
(18) Hauwiller, M. R.; Zhang, X.; Liang, W.-I.; Chiu, C.-H.; Zhang, Q.; Zheng, W.; Ophus, C.; Chan, E. M.; Czarnik, C.; Pan, M.; Ross, F. M.; Wu, W.-W.; Chu, Y.-H.; Asta, M.; Voorhees, P. W.; Alivisatos, A. P.; Zheng, H. Dynamics of Nanoscale Dendrite Formation in Solution Growth Revealed Through in Situ Liquid Cell Electron Microscopy. *Nano Lett.* **2018**, *18* (10), 6427−6433.
(19) Woehl, T. J.; Evans, J. E.; Arslan, I.; Ristenpart, W. D.; Browning, N. D. Direct in Situ Determination of the Mechanisms Controlling Nanoparticle Nucleation and Growth. *ACS Nano* **2012**, *6* (10), 8599−8610.
(20) Liao, H.-G.; Zherebetskyy, D.; Xin, H.; Czarnik, C.; Ercius, P.; Elmlund, H.; Pan, M.; Wang, L.-W.; Zheng, H. Facet Development during Platinum Nanocube Growth. *Science* **2014**, *345* (6199), 916−919.
(21) Jiang, Y.; Zhu, G.; Lin, F.; Zhang, H.; Jin, C.; Yuan, J.; Yang, D.; Zhang, Z. In Situ Study of Oxidative Etching of Palladium Nanocrystals by Liquid Cell Electron Microscopy. *Nano Lett.* **2014**, *14* (7), 3761−3765.
(22) Wu, J.; Gao, W.; Yang, H.; Zuo, J.-M. Dissolution Kinetics of Oxidative Etching of Cubic and Icosahedral Platinum Nanoparticles Revealed by in Situ Liquid Transmission Electron Microscopy. *ACS Nano* **2017**, *11* (2), 1696−1703.
(23) Ye, X.; Jones, M. R.; Frechette, L. B.; Chen, Q.; Powers, A. S.; Ercius, P.; Dunn, G.; Rotskoff, G. M.; Nguyen, S. C.; Adiga, V. P.; Zettl, A.; Rabani, E.; Geissler, P. L.; Alivisatos, A. P. Single-Particle Mapping of Nonequilibrium Nanocrystal Transformations. *Science* **2016**, *354* (6314), 874−877.
(24) Hauwiller, M. R.; Frechette, L. B.; Jones, M. R.; Ondry, J. C.; Rotskoff, G. M.; Geissler, P.; Alivisatos, A. P. Unraveling Kinetically-Driven Mechanisms of Gold Nanocrystal Shape Transformations Using Graphene Liquid Cell Electron Microscopy. *Nano Lett.* **2018**, *18* (9), 5731−5737.
(25) Tan, S. F.; Anand, U.; Mirsaidov, U. Interactions and Attachment Pathways between Functionalized Gold Nanorods. *ACS Nano* **2017**, *11* (2), 1633−1640.
(26) Yuk, J. M.; Park, J.; Ercius, P.; Kim, K.; Hellebusch, D. J.; Crommie, M. F.; Lee, J. Y.; Zettl, A.; Alivisatos, A. P. High-Resolution EM of Colloidal Nanocrystal Growth Using Graphene Liquid Cells. *Science* **2012**, *336* (6077), 61−64.
(27) Li, D.; Nielsen, M. H.; Lee, J. R. I.; Frandsen, C.; Banfield, J. F.; De Yoreo, J. J. Direction-Specific Interactions Control Crystal Growth by Oriented Attachment. *Science* **2012**, *336* (6084), 1014−1018.
(28) Park, J.; Zheng, H.; Lee, W. C.; Geissler, P. L.; Rabani, E.; Alivisatos, A. P. Direct Observation of Nanoparticle Superlattice Formation by Using Liquid Cell Transmission Electron Microscopy. *ACS Nano* **2012**, *6* (3), 2078−2085.
(29) Tan, S. F.; Chee, S. W.; Lin, G.; Mirsaidov, U. Direct Observation of Interactions between Nanoparticles and Nanoparticle Self-Assembly in Solution. *Acc. Chem. Res.* **2017**, *50* (6), 1303−1312.
(30) Sutter, E.; Sutter, P.; Tkachenko, A. V.; Krahne, R.; de Graaf, J.; Arciniegas, M.; Manna, L. In Situ Microscopy of the Self-Assembly of Branched Nanocrystals in Solution. *Nat. Commun.* **2016**, *7*, 11213.
(31) Kelly, D. J.; Zhou, M.; Clark, N.; Hamer, M. J.; Lewis, E. A.; Rakowski, A. M.; Haigh, S. J.; Gorbachev, R. V. Nanometer Resolution Elemental Mapping in Graphene-Based TEM Liquid Cells. *Nano Lett.* **2018**, *18* (2), 1168−1174.
(32) Textor, M.; de Jonge, N. Strategies for Preparing Graphene Liquid Cells for Transmission Electron Microscopy. *Nano Lett.* **2018**, *18* (6), 3313−3321.
(33) Wadell, C.; Inagaki, S.; Nakamura, T.; Shi, J.; Nakamura, Y.; Sannomiya, T. Nanocuvette: A Functional Ultrathin Liquid Container for Transmission Electron Microscopy. *ACS Nano* **2017**, *11* (2), 1264−1272.
(34) Tan, S. F.; Bisht, G.; Anand, U.; Bosman, M.; Yong, X. E.; Mirsaidov, U. In Situ Kinetic and Thermodynamic Growth Control of Au−Pd Core−Shell Nanoparticles. *J. Am. Chem. Soc.* **2018**, *140* (37), 11680−11685.
(35) Yesibolati, M. N.; Sun, H.; Canepa, S.; Lagana, S.; Kasama, T.; Kathmann, S.; Alloyeau, D.; Mølhave, K. Developing New Measurement Capabilities with Nanochannel Liquid Phase TEM. *Microsc. Microanal.* **2018**, *24* (S1), 256−257.
(36) Rehn, S. M.; Jones, M. R. New Strategies for Probing Energy Systems with In Situ Liquid-Phase Transmission Electron Microscopy. *ACS Energy Lett.* **2018**, *3* (6), 1269−1278.
(37) Woehl, T. J.; Jungjohann, K. L.; Evans, J. E.; Arslan, I.; Ristenpart, W. D.; Browning, N. D. Experimental Procedures to Mitigate Electron Beam Induced Artifacts during in Situ Fluid Imaging of Nanomaterials. *Ultramicroscopy* **2013**, *127*, 53−63.
(38) Cho, H.; Jones, M. R.; Nguyen, S.; Hauwiller, M. R.; Zettl, A.; Alivisatos, P. The Use of Graphene and Its Derivatives for Liquid Phase Transmission Electron Microscopy of Radiation-Sensitive Specimens. *Nano Lett.* **2017**, *17* (1), 414−420.
(39) Belloni, J.; Mostafavi, M.; Remita, H.; Marignier, J.-L.; Delcourt, M.-O. Radiation-Induced Synthesis of Mono- and Multi-Metallic Clusters and Nanocolloids. *New J. Chem.* **1998**, *22* (11), 1239−1255.
(40) Le Caër, S. Water Radiolysis: Influence of Oxide Surfaces on H2 Production under Ionizing Radiation. *Water* **2011**, *3* (4), 235−253.
(41) Hermannsdörfer, J.; de Jonge, N.; Verch, A. Electron Beam Induced Chemistry of Gold Nanoparticles in Saline Solution. *Chem. Commun.* **2015**, *51* (91), 16393−16396.
(42) Zhang, Y.; Keller, D.; Rossell, M. D.; Erni, R. Formation of Au Nanoparticles in Liquid Cell Transmission Electron Microscopy: From a Systematic Study to Engineered Nanostructures. *Chem. Mater.* **2017**, *29* (24), 10518−10525.
(43) Soroushian, B.; Lampre, I.; Belloni, J.; Mostafavi, M. Radiolysis of Silver Ion Solutions in Ethylene Glycol: Solvated Electron and Radical Scavenging Yields. *Radiat. Phys. Chem.* **2005**, *72* (2−3), 111−118.
(44) Yamamoto, H.; Kozawa, T.; Tagawa, S.; Naito, M.; Marignier, J.-L.; Mostafavi, M.; Belloni, J. Radiation-Induced Synthesis of Metal Nanoparticles in Ethers THF and PGMEA. *Radiat. Phys. Chem.* **2013**, *91*, 148−155.
(45) Abellan, P.; Parent, L. R.; Al Hasan, N.; Park, C.; Arslan, I.; Karim, A. M.; Evans, J. E.; Browning, N. D. Gaining Control over Radiolytic Synthesis of Uniform Sub-3-Nanometer Palladium Nano-

DOI: 10.1021/jacs.9b00082
J. Am. Chem. Soc. XXXX, XXX, XXX−XXX

particles: Use of Aromatic Liquids in the Electron Microscope. *Langmuir* **2016**, *32* (6), 1468−1477.
(46) Schneider, N. M.; Norton, M. M.; Mendel, B. J.; Grogan, J. M.; Ross, F. M.; Bau, H. H. Electron−Water Interactions and Implications for Liquid Cell Electron Microscopy. *J. Phys. Chem. C* **2014**, *118* (38), 22373−22382.
(47) Park, J. H.; Schneider, N. M.; Grogan, J. M.; Reuter, M. C.; Bau, H. H.; Kodambaka, S.; Ross, F. M. Control of Electron Beam-Induced Au Nanocrystal Growth Kinetics through Solution Chemistry. *Nano Lett.* **2015**, *15* (8), 5314−5320.
(48) Wang, M.; Park, C.; Woehl, T. J. Quantifying the Nucleation and Growth Kinetics of Electron Beam Nanochemistry with Liquid Cell Scanning Transmission Electron Microscopy. *Chem. Mater.* **2018**, *30* (21), 7727−7736.
(49) Ruditskiy, A.; Xia, Y. The Science and Art of Carving Metal Nanocrystals. *ACS Nano* **2017**, *11* (1), 23−27.
(50) Long, R.; Zhou, S.; Wiley, B. J.; Xiong, Y. Oxidative Etching for Controlled Synthesis of Metal Nanocrystals: Atomic Addition and Subtraction. *Chem. Soc. Rev.* **2014**, *43* (17), 6288.
(51) Zhang, J.; Feng, C.; Deng, Y.; Liu, L.; Wu, Y.; Shen, B.; Zhong, C.; Hu, W. Shape-Controlled Synthesis of Palladium Single-Crystalline Nanoparticles: The Effect of HCl Oxidative Etching and Facet-Dependent Catalytic Properties. *Chem. Mater.* **2014**, *26* (2), 1213−1218.
(52) Wang, Z.; Yang, G.; Zhang, Z.; Jin, M.; Yin, Y. Selectivity on Etching: Creation of High-Energy Facets on Copper Nanocrystals for CO2 Electrochemical Reduction. *ACS Nano* **2016**, *10* (4), 4559−4564.
(53) Hauwiller, M. R.; Ondry, J. C.; Alivisatos, A. P. Using Graphene Liquid Cell Transmission Electron Microscopy to Study in Situ Nanocrystal Etching. *J. Visualized Exp.* **2018**, 135, DOI: 10.3791/57665.
(54) Nikoobakht, B.; El-Sayed, M. A. Preparation and Growth Mechanism of Gold Nanorods (NRs) Using Seed-Mediated Growth Method. *Chem. Mater.* **2003**, *15* (10), 1957−1962.
(55) O'Brien, M. N.; Jones, M. R.; Brown, K. A.; Mirkin, C. A. Universal Noble Metal Nanoparticle Seeds Realized Through Iterative Reductive Growth and Oxidative Dissolution Reactions. *J. Am. Chem. Soc.* **2014**, *136* (21), 7603−7606.
(56) Bergerhoff, G.; Brown, I. D.; Allen, F. H. Crystallographic Databases. *Int. Union Crystallogr. Chester* **1987**, *360*, 77−95.
(57) Christensen, H.; Christensen, A. N.; Turpeinen, U.; Andresen, A. F.; Smidsrød, O.; Pontchour, C.-O.; Phavanantha, P.; Pramatus, S.; Cyvin, B. N.; Cyvin, S. J. Hydrogen Bonds of Gamma-FeOOH. *Acta Chem. Scand.* **1978**, *32a*, 87−88.
(58) Birch, W. D.; Pring, A.; Reller, A.; Schmalle, H. W. Bernalite, Fe(OH)3, a New Mineral from Broken Hill, New South Wales: Description and Structure. *Am. Mineral.* **1993**, *78* (7−8), 827−834.
(59) Grogan, J. M.; Schneider, N. M.; Ross, F. M.; Bau, H. H. Bubble and Pattern Formation in Liquid Induced by an Electron Beam. *Nano Lett.* **2014**, *14*, 359−364.
(60) Yang, J.; Alam, S. B.; Yu, L.; Chan, E.; Zheng, H. Dynamic Behavior of Nanoscale Liquids in Graphene Liquid Cells Revealed by in Situ Transmission Electron Microscopy. *Micron* **2019**, *116* (August 2018), 22−29.
(61) Lingane, J. J. Standard Potentials of Half-Reactions Involving + 1 and + 3 Gold in Chloride Medium. *J. Electroanal. Chem.* **1962**, *4* (6), 332−342.
(62) Whittemore, D. O.; Langmuir, D. Standard Electrode Potential of Fe3+ + E- = Fe2+ from 5−35 C. *J. Chem. Eng. Data* **1972**, *17* (3), 288−290.
(63) Skibsted, L. H.; Bjerrum, J. Standard Electrode-Potentials of Gold Aqua Ions and Stabilities of Gold (I) and Gold (III) Complexes in Aqueous-Solution. *J. Indian Chem. Soc.* **1977**, *54* (1−3), 102−108.
(64) Jordan, J.; Parsons, R.; Bard, A. J. In *Standard Potentials in Aqueous Solution*; Bard, A. J., Parsons, R., Jordan, J., Eds.; Monographs in Electroanalytical Chemistry and Electrochemistry; Marcel Dekker: New York, 1985.
(65) Legrini, O.; Oliveros, E.; Braun, A. M. Photochemical Processes for Water Treatment. *Chem. Rev.* **1993**, *93* (2), 671−698.
(66) Wu, J.; Gao, W.; Wen, J.; Miller, D. J.; Lu, P.; Zuo, J.; Yang, H. Growth of Au on Pt Icosahedral Nanoparticles Revealed by Low-Dose In Situ TEM. *Nano Lett.* **2015**, *15* (4), 2711−2715.
(67) Pashley, R. M.; Israelachvili, J. N. A Comparison of Surface Forces and Interfacial Properties of Mica in Purified Surfactant Solutions. *Colloids Surf.* **1981**, *2* (2), 169−187.
(68) Israelachvili, J. N.; Pashley, R. M. Molecular Layering of Water at Surfaces and Origin of Repulsive Hydration Forces. *Nature* **1983**, *306* (5940), 249−250.
(69) White, E. R.; Mecklenburg, M.; Singer, S. B.; Aloni, S.; Regan, B. C. Imaging Nanobubbles in Water with Scanning Transmission Electron Microscopy. *Appl. Phys. Express* **2011**, *4* (5), 055201.
(70) Shin, D.; Park, J. B.; Kim, Y. J.; Kim, S. J.; Kang, J. H.; Lee, B.; Cho, S. P.; Hong, B. H.; Novoselov, K. S. Growth Dynamics and Gas Transport Mechanism of Nanobubbles in Graphene Liquid Cells. *Nat. Commun.* **2015**, *6* (1), 6068.
(71) Park, J. B.; Shin, D.; Kang, S.; Cho, S. P.; Hong, B. H. Distortion in Two-Dimensional Shapes of Merging Nanobubbles: Evidence for Anisotropic Gas Flow Mechanism. *Langmuir* **2016**, *32* (43), 11303−11308.
(72) Mehdi, B. L.; Qian, J.; Nasybulin, E.; Park, C.; Welch, D. A.; Faller, R.; Mehta, H.; Henderson, W. A.; Xu, W.; Wang, C. M.; Evans, J. E.; Liu, J.; Zhang, J. G.; Mueller, K. T.; Browning, N. D. Observation and Quantification of Nanoscale Processes in Lithium Batteries by Operando Electrochemical (S)TEM. *Nano Lett.* **2015**, *15* (3), 2168−2173.
(73) Bouniol, P. The Influence of Iron on Water Radiolysis in Cement-Based Materials. *J. Nucl. Mater.* **2010**, *403* (1−3), 167−183.
(74) Fenton, H. J. H. Oxidation of Tartaric Acid in Presence of Iron. *J. Chem. Soc., Trans.* **1894**, *65*, 899−910.
(75) Haber, F.; Weiss, J. The Catalytic Decomposition of Hydrogen Peroxide by Iron Salts. *Proc. R. Soc. A Math. Phys. Eng. Sci.* **1934**, *147* (861), 332−351.
(76) Pignatello, J. J.; Oliveros, E.; MacKay, A. Advanced Oxidation Processes for Organic Contaminant Destruction Based on the Fenton Reaction and Related Chemistry. *Crit. Rev. Environ. Sci. Technol.* **2006**, *36* (1), 1−84.
(77) Buxton, G. V.; Greenstock, C. L.; Helman, W. P.; Ross, A. B. Critical Review of Rate Constants for Reactions of Hydrated Electrons, Hydrogen Atoms and Hydroxyl Radicals (·OH/·O −) in Aqueous Solution. *J. Phys. Chem. Ref. Data* **1988**, *17* (2), 513−886.
(78) Ruppert, G.; Bauer, R.; Heisler, G. The Photo-Fenton Reaction - an Effective Photochemical Wastewater Treatment Process. *J. Photochem. Photobiol., A* **1993**, *73* (1), 75−78.
(79) Ni, W.; Kou, X.; Yang, Z.; Wang, J. Tailoring Longitudinal Surface Plasmon Wavelengths, Scattering and Absorption Cross Sections of Gold Nanorods. *ACS Nano* **2008**, *2* (4), 677−686.
(80) Zou, R.; Guo, X.; Yang, J.; Li, D.; Peng, F.; Zhang, L.; Wang, H.; Yu, H. Selective Etching of Gold Nanorods by Ferric Chloride at Room Temperature. *CrystEngComm* **2009**, *11* (12), 2797.

DOI: 10.1021/jacs.9b00082
J. Am. Chem. Soc. XXXX, XXX, XXX−XXX